Research in Astronomy and Astrophysics, 23:105005 (12pp), 2023 October https://doi.org/10.1088/1674-4527/ace179
© 2023. National Astronomical Observatories, CAS and IOP Publishing Ltd. Printed in China and the U.K.

Reciprocating Magnetic Fields in the Pulsar Wind Observed from the Black Widow Pulsar J1720-0534

Chen-Chen Miao[1,2], Victoria Blackmon[3], Wei-Wei Zhu[1,4], Dong-Zi Li[5], Ming-Yu Ge[6], Xiao-Peng You[7], Maura McLaughlin[3], Di Li[1,8], Na Wang[9], Pei Wang[1,4], Jia-Rui Niu[1,2], M. Cruces[10], Jian-Ping Yuan[9], Jun-Tao Bai[9], D. J. Champion[10], Yu-Tong Chen[1,2], Ming-Min Chi[11], P. C. C. Freire[10], Yi Feng[8], Zhen-Ye Gan[12], M. Kramer[10], Fei-Fei Kou[9], Yu-Xi Li[12], Xue-Li Miao[1], Ling-Qi Meng[1,2], Chen-Hui Niu[1,13], Sheng-Nan Sun[9], Zhong-Yi Sun[12], H. M. Tedila[9], Shuang-Qiang Wang[9], Qing-Dong Wu[9], Jing-Bo Wang[14], Zhi-Gang Wen[9], Shen Wang[11], Ya-Biao Wang[12], Cheng-Jie Wang[12], Meng-Yao Xue[1], You-Ling Yue[1], Mao Yuan[1,2], Ju-Mei Yao[9], Wen-Ming Yan[9], Ru-Shuang Zhao[1,15], Lei Zhang[1], and De Zhao[9]

[1] National Astronomical Observatories, Chinese Academy of Sciences, Beijing 100101, China; zhuww@nao.cas.cn
[2] School of Astronomy and Space Science, University of Chinese Academy of Sciences, Beijing 100049, China
[3] West Virginia University, 1500 University Ave, Morgantown, WV 26506, USA
[4] Institute for Frontiers in Astronomy and Astrophysics, Beijing Normal University, Beijing 102206, China
[5] Cahill Center for Astronomy and Astrophysics, California Institute of Technology, 1216 E California Boulevard, Pasadena, CA 91125, USA
[6] Key Laboratory of Particle Astrophysics, Institute of High Energy Physics, Chinese Academy of Sciences, Beijing 100049, China
[7] School of Physical Science and Technology, Southwest University, Chongqing 400715, China
[8] Research Center for Intelligent Computing Platforms, Zhejiang Laboratory, Hangzhou 311100, China
[9] Xinjiang Astronomical Observatory, Chinese Academy of Sciences, Urumqi 830011, China
[10] Max-Planck Institut für Radioastronomie, Auf dem Hügel 69, D-53121 Bonn, Germany
[11] School of Computer Science, Fudan University, Shanghai 200433, China
[12] Tencent Youtu Lab, Shanghai 200233, China
[13] College of Physical Science and Technology, Central China Normal University, Wuhan 430079, China
[14] Institute of Optoelectronic Technology, Lishui University, Lishui 323000, China
[15] Guizhou Normal University, Guiyang 550001, China
Received 2023 March 30; revised 2023 April 20; accepted 2023 April 24; published 2023 September 19

Abstract

We report the radio observations of the eclipsing black widow pulsar J1720−0534, a 3.26 ms pulsar in orbit with a low mass companion of mass 0.029 to 0.034 $M_\odot$. We obtain the phase-connected timing ephemeris and polarization profile of this millisecond pulsar (MSP) using the Five-hundred-meter Aperture Spherical radio Telescope (FAST), the Green Bank Telescope (GBT), and the Parkes Telescope. For the first time from such a system, an oscillatory polarization angle change was observed from a particular eclipse egress with partial depolarization, indicating 10-milliGauss-level reciprocating magnetic fields oscillating in a length scale of 5×10^3 km (assuming an orbital inclination angle of 90°) outside the companion's magnetosphere. The dispersion measure variation observed during the ingresses and egresses shows the rapid raising of the electron density in the shock boundary between the companion's magnetosphere and the surrounding pulsar wind. We suggest that the observed oscillatory magnetic fields originate from the pulsar wind outside the companion's magnetosphere.

Key words: (stars:) pulsars: general – (stars:) pulsars: individual (J1720-0534) – (stars:) binaries: eclipsing

1. Introduction

Spider pulsars are millisecond pulsars (MSPs) orbiting low-mass companions ($M_C < 1\,M_\odot$) in tight orbital periods ($P_b <$ 24 hr) (Roberts 2011, 2013). There are two explicit subgroups of spider pulsars (Roberts 2011): black widows (BWs) have likely-degenerate companions with mass $M_C < 0.05\,M_\odot$, and redbacks (RBs) have non-degenerate companions with mass $M_C \sim 0.1$–$1.0\,M_\odot$. Spider pulsar systems commonly show eclipsing behaviors like: frequency-dependent radio intensity eclipse wider than the companion physical size (Fruchter et al. 1988; Polzin et al. 2018) and linear polarization eclipse leading and trailing the intensity eclipse by a few degrees (You et al. 2018; Li et al. 2023; Crowter et al. 2020).

The magnetic field in the eclipse medium causes the polarization eclipse of spider pulsars (Thompson et al. 1994; Kansabanik et al. 2021). As suggested by Thompson et al. (1994) and Polzin et al. (2018), the eclipsing materials should contain $\gtrsim$10 G magnetic field to balance the energy density in the pulsar relativistic-particle wind. The recent result of PSR J1544+4937 also shows that eclipsing material needs to contain ∼10 G magnetic field from wide-band flux intensity modeling (Kansabanik et al. 2021). However, observations of the depolarization eclipse do not always agree with the prediction above. Based on the plasma lensing argument, the average magnetic field parallel to the line-of-sight (LOS) $\langle B_\parallel \rangle$ for PSR B1957+20 is 0.02 ± 0.09 G (Li et al. 2019). Crowter et al. (2020) measure a corresponding $B_\parallel \sim 3.5 \pm 1.7$ mG

at the eclipse egress of PSR J2256−1024 through polarization angle changes caused by Faraday rotation. Other indirect evidences point to a higher magnetic field strength in the eclipsing materials. Li et al. (2023) measure substantial rotation measure (RM) changes over particular orbital phases away from the eclipse and changes of circular polarization consistent with the synchrotron-cyclotron absorption caused by magnetic fields of 10-100 G from PSR 1744-24A.

PSR J1720−0534 (Wang et al. 2021) is a Galactic field BW pulsar with a spin period of 3.26 ms discovered in the Commensal Radio Astronomy FAST Survey (CRAFTS) (Li et al. 2018; Cameron et al. 2020; Cruces et al. 2021; Miao et al. 2023). The discovery of this BW pulsar and the presentation of pulse intensity variation with a modulation period of ∼22 s during the ingress of the eclipse have been reported (Wang et al. 2021). In this work, we report the phase-connected timing ephemeris, polarization profile, and a magnetic field reversal of this pulsar. In Section 2, we present the radio observations and data analyses. In Section 3, we describes our timing results, linear polarization variation with the orbital phase, and a only magnetic field reversal in an observation. We discuss and summarize our results in Section 4.

2. Observation and Data Analysis

2.1. Observation

There were 42 observations performed at FAST with its 19-beam L-band receiver (Nan et al. 2011; Jiang et al. 2020), which covers a frequency band of 1.0−1.5 GHz. To ensure the possible smallest data sizes, we used two different observation modes. The regular timing observations were carried out with 1024 frequency channels and 49.152 μs sampling time. The analysis of DM and RM variation was carried out with 8192 frequency channels and a sampling time of 98.304 μs. The observations at the 100 m Green Bank Telescope (GBT) were carried out using the 350 MHz and 820 MHz feeds at its prime focus receiver. Data were coherently de-dispersed using the VEGAS backend at a DM of 37.8 pc cm^{-3} with 128 frequency channels, and sampling times of 20.48 μs and 10.24 μs at 350 and 820 MHz, respectively. The observation taken at the Parkes telescope was made with the ultra-wide-bandwidth low-frequency (UWL) receiver (Hobbs et al. 2020). This 2.7 hr observation covered ∼90% of the orbital phase. All the data presented in this work were recorded in pulsar search mode with full polarimetry. The parameters of timing observations and eclipsing events are listed in Table A1.

2.2. Data Processing

The initial timing ephemeris was derived with tools from PRESTO[16] (Ransom 2011). We folded the data with the initial ephemeris by using DSPSR[17] (van Straten & Bailes 2011) and obtained the pulse time of arrivals (ToAs) with PSRCHIVE[18] (Hotan et al. 2004) software packages. We used TEMPO[19] (Nice et al. 2015) and DRACULA[20] (Freire & Ridolfi 2018) to get a phase-connected timing solution with the initial ephemeris and these ToAs. After obtaining a phase-connected timing solution, we refolded the data and performed the polarimetric calibration on the newly folded data. We derived the new ToAs with PSRCHIVE and get the timing residuals by using TEMPO. ToA integration

Table 1
Best-fit TEMPO Timing Parameters for Pulsar J1720-0534

Pulsar name	J1720-0534
Measured Parameters	
R.A., α (J2000) …	17:20:54.505914(2)
decl., δ (J2000) …	–05:34:23.82233(14)
Spin Frequency, ν (s^{-1}) …	306.030167430858(4)
Spin frequency derivative, $\dot{\nu}$ (s^{-2}) …	$-7.6539(19) \times 10^{-16}$
Dispersion Measure, DM (cm^{-3} pc) …	36.82987(10)
Binary model …	ELL1
Orbital Period, P_b (day) …	0.13169857686(2)
Projected semimajor axis, x (lt-s) …	0.05961281(10)
Epoch of the ascending node, Tasc (MJD) …	58941.85271857(4)
$e \sin\omega$, $\epsilon_1(10^{-5})$ …	0.2(2)
$e \cos\omega$, $\epsilon_2(10^{-5})$ …	–4.3(2)
Mass function, $f(10^{-3})M_\odot$ …	0.01311331(6)
Fixed Parameters	
Solar System Ephemeris[a] …	DE438
Reference epoch for α, δ, and ν (MJD) …	58990.725174
Data span (MJD)…	58987—59626
Number of TOAs…	2697
Fit χ^2/number of degrees of freedom…	5524.72/2688
Post-fit rms of residuals (μs)…	3.093
EFAC…	1.43
Derived Parameters	
Minimum companion mass[b], $m_{c,min}(M_\odot)$ …	0.029
Median companion mass[c], $m_{c,med}(M_\odot)$ …	0.034
Inferred eccentricity, e (10^{-5}) …	4.3(2)
Galactic longitude, l (°) …	17.0667302186(7)
Galactic latitude, b (°) …	17.25223302(4)
Spin-down luminosity, $\dot{E}$ (10^{33} erg s^{-1}) …	9.2
Surface magnetic field, B_{surf} (10^8 G) …	1.6
Characteristic age, τ_c (Gyr) …	6.3

Notes.
[a] The timing model use the DE438 solar system ephemeris and is referenced to the TT(BIPM) time standard. Values in parentheses are the 1σ uncertainty in the last digit as reported by TEMPO.
[b] $m_{c,min}$ is calculated for an orbital inclination of $i = 90°$ and an assumed pulsar mass of 1.35 $M_\odot$ (Hobbs et al. 2006).
[c] $m_{c,med}$ is calculated for an orbital inclination of $i = 60°$ and an assumed pulsar mass of 1.35 $M_\odot$ (Hobbs et al. 2006).

[16] https://github.com/scottransom/presto
[17] http://dspsr.sourceforge.net
[18] http://psrchive.sourceforge.net
[19] http://tempo.sourceforge.net
[20] https://github.com/pfreire163/Dracula

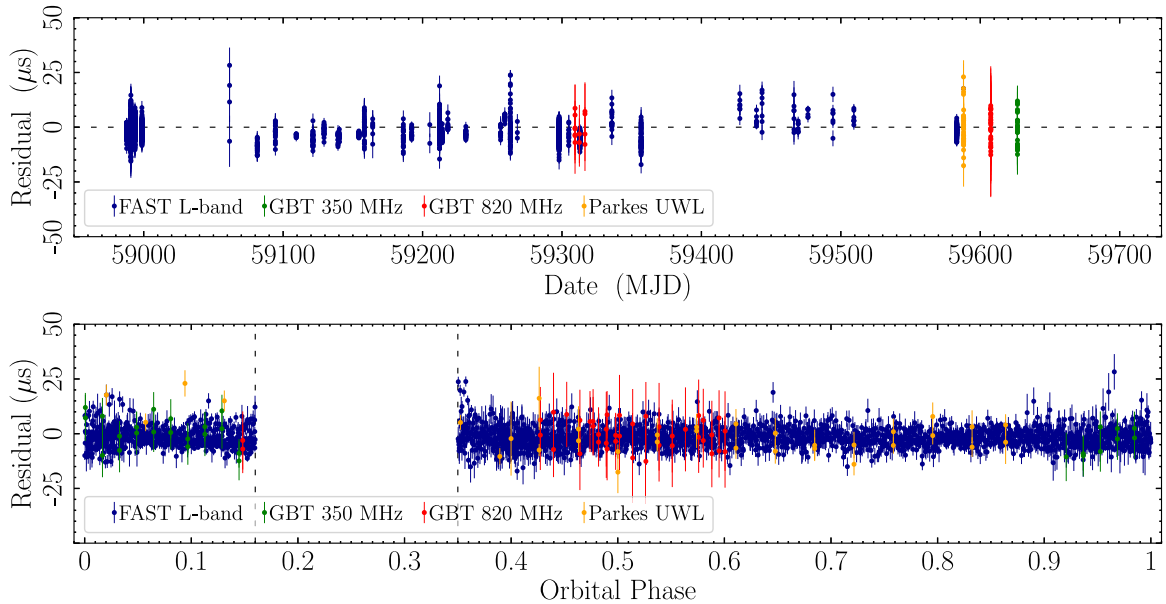

Figure 1. Post-fit timing residuals of all observations. Upper panel: The timing residuals vs. MJD. Lower panel: The timing residuals vs. orbital phase. Residuals at 350 and 820 MHz from GBT observations are plotted in green and red, while residuals from FAST and Parkes observations are plotted in blue and yellow, respectively. The vertical lines in the lower panel represent the approximate location of the eclipse, at orbital phases between 0.16 and 0.35.

times used for FAST, GBT, and Parkes observations are is 20 s, 120 s, and 420 s, respectively.

2.3. Faraday Rotation Measurements

The observations covering the eclipses are all taken at 1250 MHz with the FAST. To study the depolarization of the pulsar signals during the eclipse phase, we search for the optimal RM using `RM-TOOLS`[21] (Purcell et al. 2020) from each sub-integration. We obtained polarization profiles with the signal-to-noise ratio ∼80 by forming profiles for every 20 s. We find $\mathrm{RM} \approx 21\,\mathrm{rad\,m^{-2}}$ at the non-eclipsing phases ($0.00 < \phi_b < 0.15$ and $0.40 < \phi_b < 1.00$).

The `RM-TOOLS` failed to provide a fit result for the ingress and egress phase ($0.15 < \phi < 0.18$ and $0.31 < \phi_b < 0.40$), due to the low linear polarization. We then attempt to obtain the RM variation by measuring the polarization position angle (PA) shift of the sub-integration (Crowter et al. 2020). The extra RM is given by $\Delta\mathrm{RM} = \Delta\mathrm{PA}\, f_c^2\, c^{-2}$, where ΔPA is the PA shift; c is the speed of light in $\mathrm{m\,s^{-1}}$; and $f_c = 1250$ MHz is the center frequency of the observation. We compare PA values between the shifted and non-shifted PA profiles to obtain the ΔPA measurements.

3. Results

We present a phase-connected timing solution for PSR J1720−0534 (Table 1) based on two years of observations. This 3.26 ms pulsar is in a tight orbit with an orbital period of 3.16 hr, an eccentricity of 4.4×10^{-5}, and a projected semimajor axis of 0.0596 lt-s. The companion mass is to be between $0.029-0.068\,M_\odot$, assuming $90° \geqslant i \geqslant 26°$ and a pulsar mass of $1.35\,M_\odot$. We derive the spin-down luminosity ($\dot{E}$), the surface magnetic field ($B_{\rm surf}$), and the characteristic age (τ_c) from the intrinsic period (P) and spin period derivative ($\dot{P}$). The $\dot{E}$ of 9×10^{33} $\mathrm{erg\,s^{-1}}$ is similar to those of the 102 published LAT-detections of Gamma-Ray MSPs[22] with measured $\dot{E}$. We folded the 12-year Fermi-LAT data with the timing solution in Table 1, but no pulse was detected. We searched the potential counterpart at the Gaia DR3 catalogs (Gaia Collaboration et al. 2021) and none was found within a 1″ radius.

Figure 1 shows the post-fit timing residuals as the function of orbital phases (ϕ_b) and MJDs, with different colors representing different telescopes. The eclipse and its surroundings have been excluded ($0.16 < \phi_b < 0.35$, by eyes). The post-fit weighted rms (WRMS) of timing residuals is 3.093 μs after applying an error factor (EFAC) of 1.43.

We present the variation of the excess DM (ΔDM) and the inferred excess electron column density (N_e) of 10 eclipse observations in Figure 2, with different colors representing different observations. These observations, which cover the phase of the eclipse, were all made with the FAST telescope. On MJD 58987 and MJD 59262, we detect two significant DM

[21] https://github.com/CIRADA-Tools/RM-Tools

[22] https://confluence.slac.stanford.edu/display/GLAMCOG/Public+List+of+LAT-Detected+Gamma-Ray+Pulsars

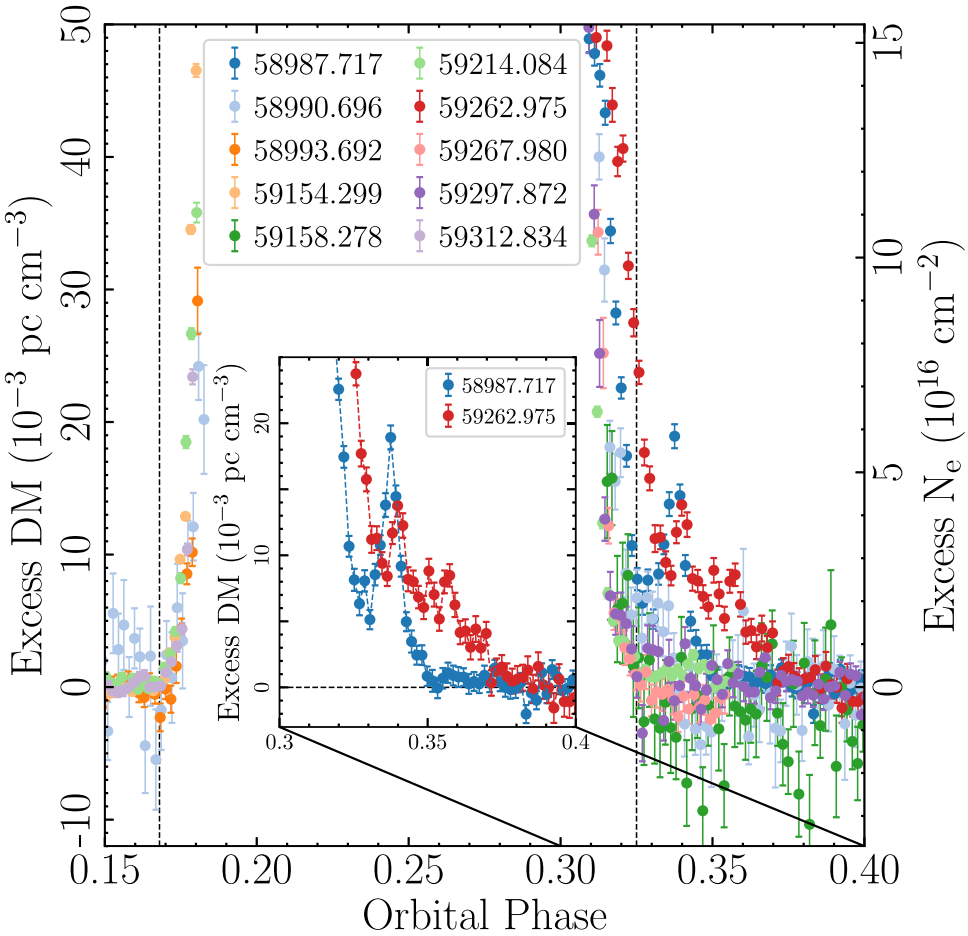

Figure 2. Variations of the excess DM (ΔDM) and excess electron column densities (N_e) as the function of orbital phases around superior conjunction. Different colors represent the different eclipse observations. The inset shows the DM "blips" observed on MJD 58987 and MJD 59262.

fluctuations during the eclipse egress (called blips, Crowter et al. 2020). The close-ups of the blips are presented in the insert plot of Figure 2. The pulse profile and linear polarization position angle (PA) for PSR J1720−0534 at 350 MHz (MJD 59626) and 1250 MHz (MJD 59313) are shown in Figure 3. The pulse profile at 820 MHz is similar to the 1250 MHz one. As described in Rotating Vector Model (RVM, Radhakrishnan & Cooke 1969; Everett & Weisberg 2001), the linear polarization PA is a function of the magnetic inclination angle (α), the angle between the line of sight and the rotation axis (ζ), the reference position angle (ψ_0), and longitude of the fiducial plane (ϕ_0). We used the RVM model to model the viewing geometry of this pulsar. The geometric parameters used for RVM fits are $\alpha = 84\overset{\circ}{.}2$, $\zeta = 96\overset{\circ}{.}1$, $\psi_0 = -74\overset{\circ}{.}2$ and $\phi_0 = 221\overset{\circ}{.}8$.

The variations of ΔDM, normalized flux density and polarization fraction for five observations covering the eclipses are shown in Figure 4. At ϕ_b between 0.165 and 0.180, the circular polarization is detected while the linear polarization is depolarized. The circular polarization starts to be detected at $\phi_b = 0.31$ while the linear polarization is still depolarized. The circular polarization is eclipsed at the similar orbital phase as the total intensity, as a result the linear polarization presents a wider eclipse range, disappears earlier, and appears later.

Only at MJD 59214, we observed a shift in the PA when the linear polarization appears again in the orbital phase of 0.32—0.35 (shown in Figure 5). The flux of linear polarization shows a decrease at random decrease at different orbital phase and totally disappeared at $\phi_b = 0.324$, 0.330, 0.342, 0.344, and 0.354. The PA profiles also show the random shifts. At the same time, the total intensity profiles (I) and circular polarization profiles (V) show no deviations. The ΔDM and ΔRM measurements between the orbital phase 0.32 and 0.35 are presented in the top panel of Figure 6.

Recent research indicates that a magnetic field permeates the eclipse material being the cause of a shift in PA and linear depolarization (You et al. 2018; Crowter et al. 2020; Li et al. 2023). The average magnetic field in the eclipse material $\langle B_{\parallel} \rangle$

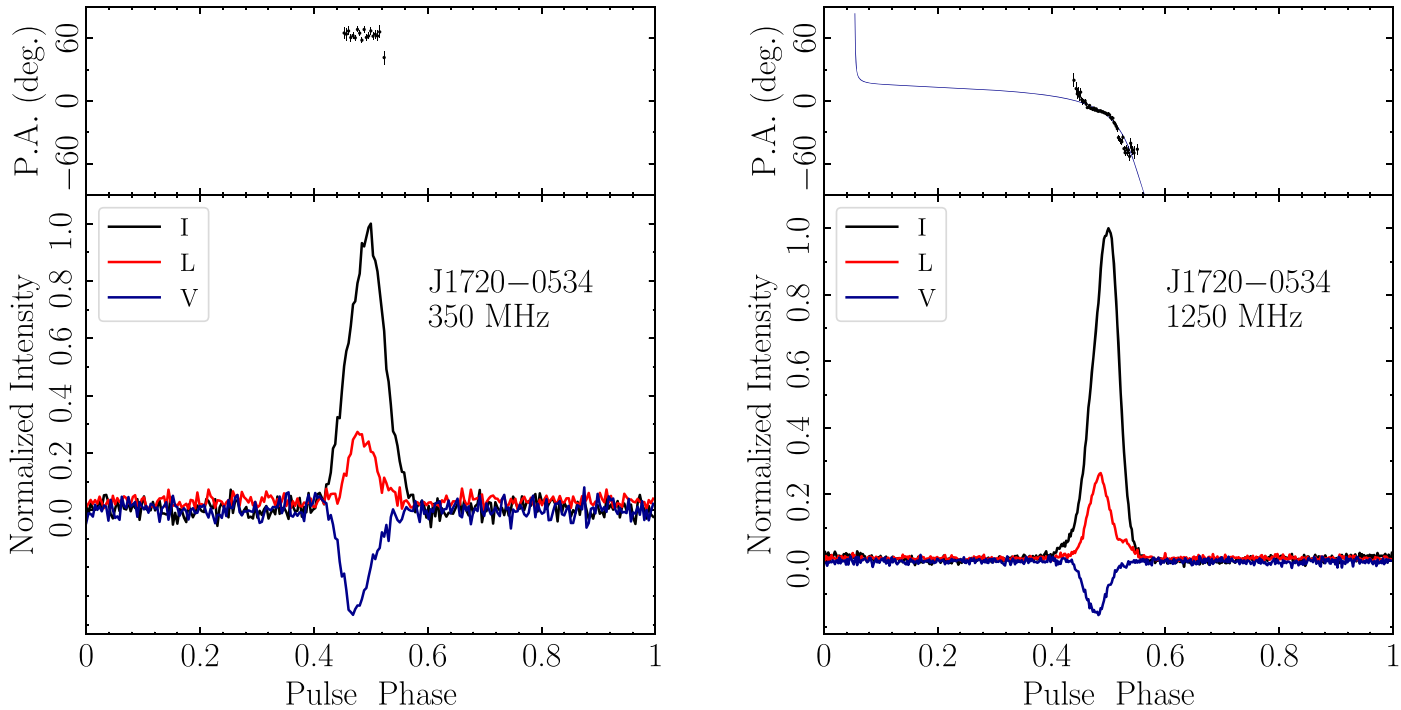

Figure 3. Pulse profile and polarization position angle for PSR J1720−0534 at 350 MHz (left) and 1250 MHz (right). The upper panel of each plot is the position angle, and the lower panel of is the polarization profiles. The blue solid line in the upper panel represents the best-fitting RVM model. The total intensity (I), linear polarization (L), and circular polarization (V) profiles are represented by black, red, and blue solid lines.

is given by Equation (1) while assuming that the ΔRM and ΔDM are originating in the same place (Crowter et al. 2020; Li et al. 2023). Positive/negative RMs indicate that the direction of $\langle B_{\parallel}\rangle$ is toward/away from the observer.

$$\langle B_{\parallel}\rangle = 1.232\ \mu\mathrm{G}\left(\frac{\Delta\mathrm{RM}}{\mathrm{rad\ m^{-2}}}\right)\left(\frac{\Delta\mathrm{DM}}{\mathrm{pc\ cm^{-3}}}\right)^{-1} \quad (1)$$

Detailed $\langle B_{\parallel}\rangle$ measurements are presented as black dots in the bottom panel of Figure 6. These ΔDM and ΔRM imply a maximum magnitude of $\langle B_{\parallel}\rangle$ toward the LOS direction of $\sim 24 \pm 8$ mG and a maximum $\langle B_{\parallel}\rangle \sim -10 \pm 5$ mG in the opposite direction.

It is worth noting that when $|\Delta\mathrm{PA}| \geqslant 90°$, it is possible that the PA would wrap around and appear on the opposite side of the baseline. This could lead to a misinterpretation of the ΔRM. However, at 1.25 GHz, a $\Delta\mathrm{RM} = 27\ \mathrm{rad\ m^{-2}}$ that lead to $|\Delta\mathrm{PA}|$ of 90° will also reduce the linear polarization fraction L_{obs} to 63% of the original level (L_{ori}) (Li et al. 2023). But the polarization reduction fractions $L_{\mathrm{obs}}/L_{\mathrm{ori}}$ measured from most of the egress phases are greater then 70%, which means that the $|\Delta\mathrm{PA}|$ at these phases should be smaller than 90°, except for $\phi_b = 0.345$, where $L_{\mathrm{obs}}/L_{\mathrm{ori}} \sim 63\%$ (the left bottom panel of Figure 5). At the orbital phase of 0.345, there are two possible values for ΔPA: $78° \pm 3°$ or $-102° \pm 3°$. A theory predicts that $L_{\mathrm{obs}}/L_{\mathrm{ori}}$ should drop to 55% if the ΔPA is −102°. This is in tension with the observed value. Therefore, we think that $\Delta\mathrm{PA} = 78° \pm 3°$ is favored for $\phi_b = 0.345$.

4. Discussion & Conclusion

In the two-year timing campaigns, we measured the astrometric parameters (RA and DEC), pulsar parameters (ν, $\dot{\nu}$, and DM), and binary parameters (P_{B}, x, T_{asc}, ϵ_1, and ϵ_2) of PSR J1720−0534 (Table 1). The measurements of the proper motion, projected semimajor axis derivative, and orbital period derivative are future objectives that could help us reveal more about the binary evolution of this system.

PSR J1720−0534 is a BW pulsar system and is eclipsed at the orbital phases of 0.19 − 0.31 (∼12% of its orbit) at L-band. Assuming $i = 90°$ and a pulsar mass of $1.35\,M_{\odot}$, the minimum pulsar-companion separation is $\sim 1.2\,R_{\odot}$ and the radius of the companion's Roche lobe (Eggleton 1983) is $R_L^c = 0.16\,R_{\odot}$. Combining the eclipse span and pulsar-companion separation, the eclipse radius R_E is $0.45\,R_{\odot}$ ($\sim 2.8\,R_L^c$) (Altamirano et al. 2011).

The intensity eclipses of PSR J1720−0534 are consistent with a symmetrical core plus variable edges. The ingresses happen at $\phi_b = 0.18$ and last for ∼1% of the orbit (half-maximum flux density). The egresses happen at the $\phi_b = 0.31$ and the egress duration varies between 1% and 2% of the orbit. The steady ingress and swept-back egress suggest that the

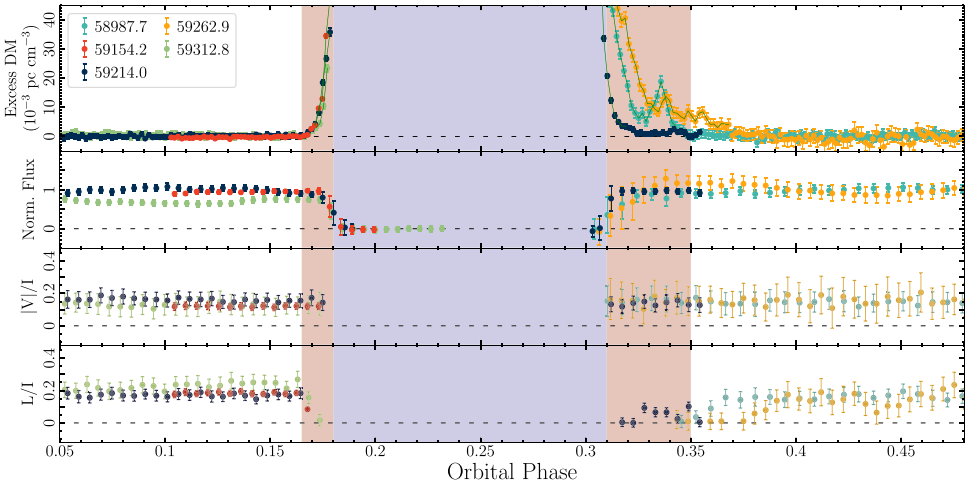

Figure 4. Variation of the ΔDM, normalized mean flux density, and polarization fractions along the eclipse. Different colors represent different observations. The upper panel with $\Delta DM \geqslant 0.006$ pc cm^{-3} in the same observation are connected by lines. The eclipse region is shaded in purple at the orbital phase between 0.18 and 0.31. The linear depolarization region is shaded in pink at orbital phases of 0.165–0.180 and 0.31–0.35.

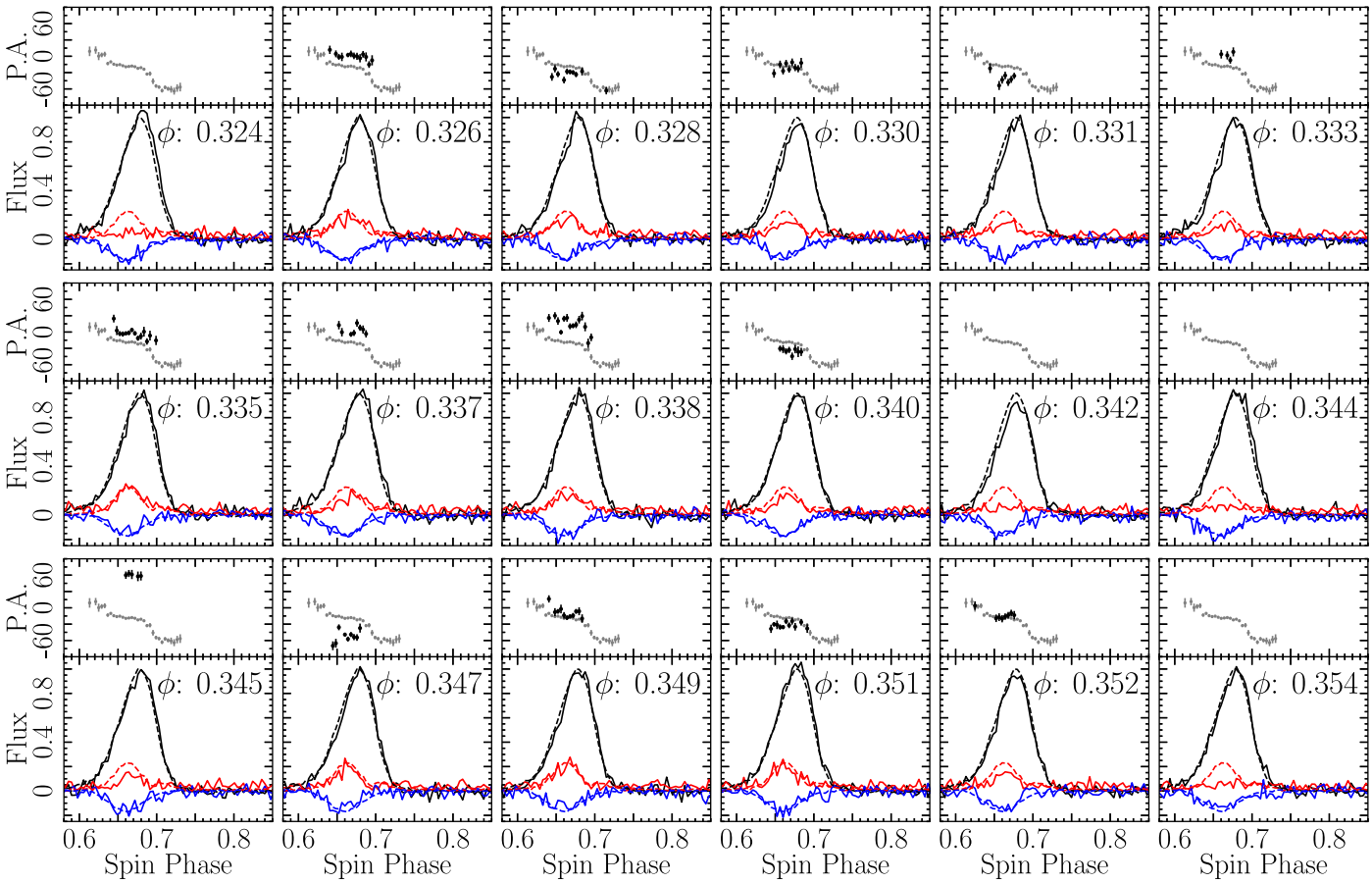

Figure 5. Sub-integration polarization profile variation in different orbital phases. The sub-integration profiles are for the integration time of 20 s for a FAST telescope observation on MJD 59214. The orbital phase (ϕ) at the center of each integration is at the top right corner of each subplot. The lower panel of the sub-plot gives the sub-integration pulse profile (solid line) comparing with the average pulse profile (dashed line) from this observation, with I, L, V profiles are plotted in black, red, and blue. the different colors representing different polarization. The position angle (PA) of the average profile comparing with the sub-integration profile are presented at the top panel.

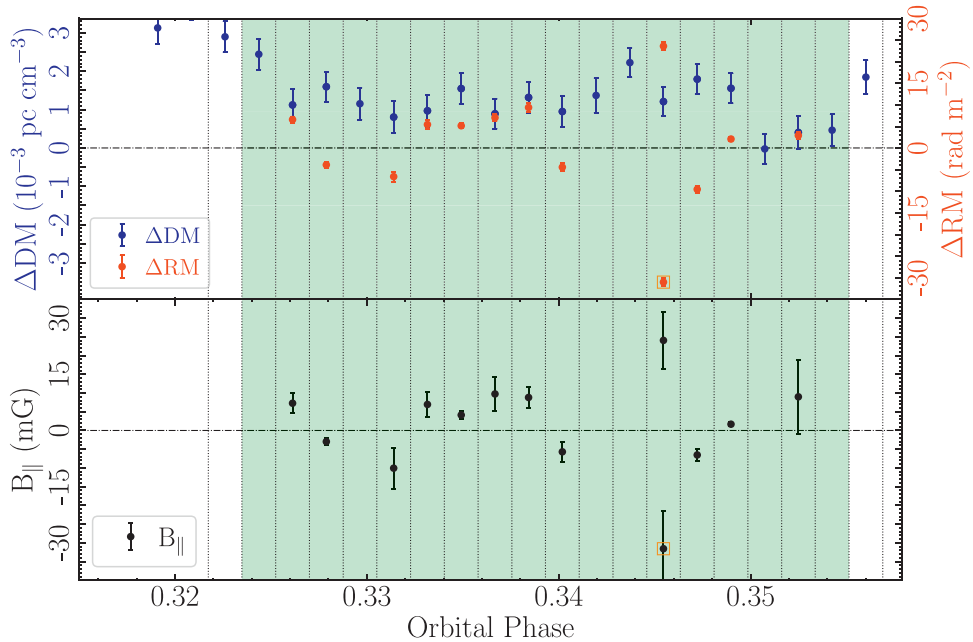

Figure 6. The detailed ΔDM (blue dots), ΔRM (red dots), and extra magnetic field strength at the LOS direction ($B_{\parallel}$, black dots). Dotted vertical lines show the division of each sub-integration and dashed horizontal lines at 0 are added for comparison. At the orbital phase of 0.345, there are two possible values for ΔRM. The ΔRM and extra magnetic field derived from the ΔPA greater than 90° are marked with orange squares.

eclipse material around the companion leaves a comet-like tail due to orbital motion.

The strength of these fields is similar to the turbulent and ordered field observed from other BW pulsar systems inferred using Faraday rotations (You et al. 2018; Polzin et al. 2019; Crowter et al. 2020; Li et al. 2023). The oscillatory magnetic field in egress is observed for the first time and presents an important piece of evidence for understanding the interactions between the pulsar and the companion.

The polarization observed in the egress phase reveals an orderly magnetic field showing an oscillatory pattern with a timescale of 20 s and direction reversal. This oscillation timescale corresponds to a length scale of $\sim 5 \times 10^3$ km when assuming an i of 90°.

We summarize the eclipsing event as follows:

1. A symmetrical complete-eclipsing body larger than the companion star in physical dimension;
2. Varying asymmetrical ingress and egress, through which the pulsar signal can pass with different levels of extra dispersion and depolarization.
3. Electron densities between 0 and $>1.3 \times 10^7$ cm^{-3} were found in the ingress and egress.
4. We find a 10-milliGauss-level reciprocating magnetic field from one of the eclipse egresses with a low electron density ($<10^6$ cm^{-3}).

Various physical pictures have been proposed in the literature to explain the eclipse of black widows and redbacks. In this paper, we explain our observations of J1720−0534 with a particular picture that was proposed as one of the possible scenarios for other BW pulsars (e.g., Phinney et al. 1988; Thompson et al. 1994; Wadiasingh et al. 2018). We suggest that the eclipse is caused by the magnetosphere of the brown dwarf. The brown dwarf magnetosphere interacts with the pulsar wind in a similar way as the Earth magnetosphere interacts with the Solar winds (Sckopke et al. 1983). There is a shock boundary between the companion magnetosphere and the pulsar wind outside. The 10-milliGauss-level reciprocating magnetic field observed in the egress is part of the pulsar wind outside of the magnetosphere.

To better illustrate our idea, we present the following three general categories of models, discuss their implications, and provide evidence that falsifies some of them and supports the other (Figure 7).

4.1. Naive Stellar Wind

An important feature of the black widow eclipse is the fact that the eclipsing body is bigger than the companion star's Roche lobe ($R_E \sim 2.8\, R_L^c$). When Fruchter et al. (1988) discovered the first black widow system B1957+20, they suggest that the eclipse could be caused by a stellar wind from the companion evaporated by the pulsar. Figure 7 illustrate an eclipsing body with an isotropic out-flowing stellar wind that surrounds the companion. The speed of the stellar wind should be far greater than the orbital velocity of the companion

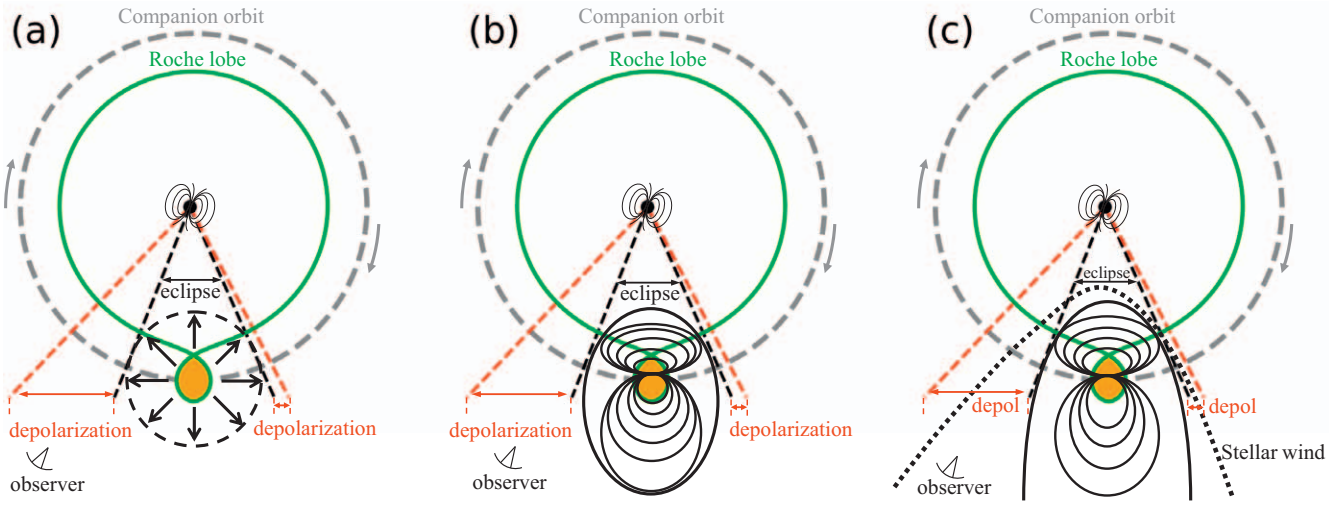

Figure 7. Three general categories of models for the eclipsing body: (a) a naive companion wind picture; (b) the companion magnetosphere; (c) the companion's magnetosphere plus a pulsar wind shock boundary. The Roche lobe and companion orbit are calculated assuming a pulsar mass of 1.35 $M_\odot$ and an orbital separation of 1.2 $R_\odot$ ($i = 90°$). The Roche lobe of the companion star is filled in yellow. The eclipse edges and linear depolarization edges are shown by black and red dashed lines. The black dashed curves represent the magnetic field and the black solid curves represent the edge of stellar wind. The gray arrows indicate the companion's direction of motion.

$V_{\rm orb} = 409$ km s^{-1} ($i = 90°$) in order to create a symmetrical eclipsing body. However, a stable isotropic wind should have a density profile of $\rho(r) \propto 1/r$ based on Gauss's theorem. Such a density profile is smooth toward the eclipsing edge, inconsistent with what was observed at the edge of the eclipsing body (Figure 8).

Note that electron density n_e is often estimated simply by taking the column density n_H derived from dispersion and dividing it with the eclipsing body diameter $2R_E$. This is a crude estimation that does not take the distance from the eclipse center into account. In Figure 8 we present n_e based on $\propto 1/r$ profile but account for the different LOS length for different eclipsing phase ϕ. This figure helps us demonstrate the discrepancy between a wind density profile and the observed density profile. But the presented n_e should also serve as a reasonably good general estimation for electron density for our later discussion.

4.2. The Companion Magnetosphere

In the other scenario (Figure 7(b)), the pulsar emission is eclipsed by the plasma in the magnetosphere of the companion. Assuming that the companion brown dwarf is Roche Lobe-filling and has a surface magnetic field of 10^3 G (Reiners & Christensen 2010), we get a magnetic field strength of 4.5×10^1 G at the eclipse edge ($\phi_b = 0.31$). A magnetosphere field strength of 10 G is sufficient to trap and dominate plasma (assuming protons and electrons) of number density $< 3 \times 10^{13}$ cm^{-3} and velocity $\sim V_{\rm orb}$.

Thompson et al. (1994) suggests that, at the edge of the magnetosphere of the brown dwarf, the magnetic pressure should balance the pulsar wind pressure, while the pulsar wind energy density is $U_E = \frac{\dot{E}}{4\pi c a^2}$ and the magnetic pressure is $\frac{B_E^2}{8\pi}$. Here $\dot{E}$ is the spin-down luminosity, c is the speed of light, a is the orbital separation, and B_E is the magnetic field of the eclipse medium. From this, the magnetic field strength of B_E should be $\approx$8 G (Wang et al. 2021).

Interestingly, the derived theoretical magnetic field strength (45 G) is more than sufficient for the required field strength (8 G) at the eclipsing edge. However, these field strengths are more than three orders of magnitude higher than the value observed in our egress (10 mG).

4.3. Pulsar Wind

The third scenario (Figure 7(c)) supplements the second one with pulsar wind and a shock boundary, and fixes the inconsistency mentioned above. Such a picture was proposed by Phinney et al. (1988) as one of the early models. In this picture, a shock boundary exists between the magnetosphere and the pulsar wind. Outside of the shock boundary are high-speed, low-density pulsar wind particles traveling with a low magnetic field, and inside, the slow-moving, high-density plasma trapped by the companion's magnetic fields. This is similar to the boundary shock observed from the solar wind and the Earth magnetosphere (Sckopke et al. 1983) where both the electron density and magnetic field rose suddenly as the ISEE-1[23] probe traveled downstream of the solar wind into the Earth magnetosphere.

[23] International Sun-Earth Explorer 1

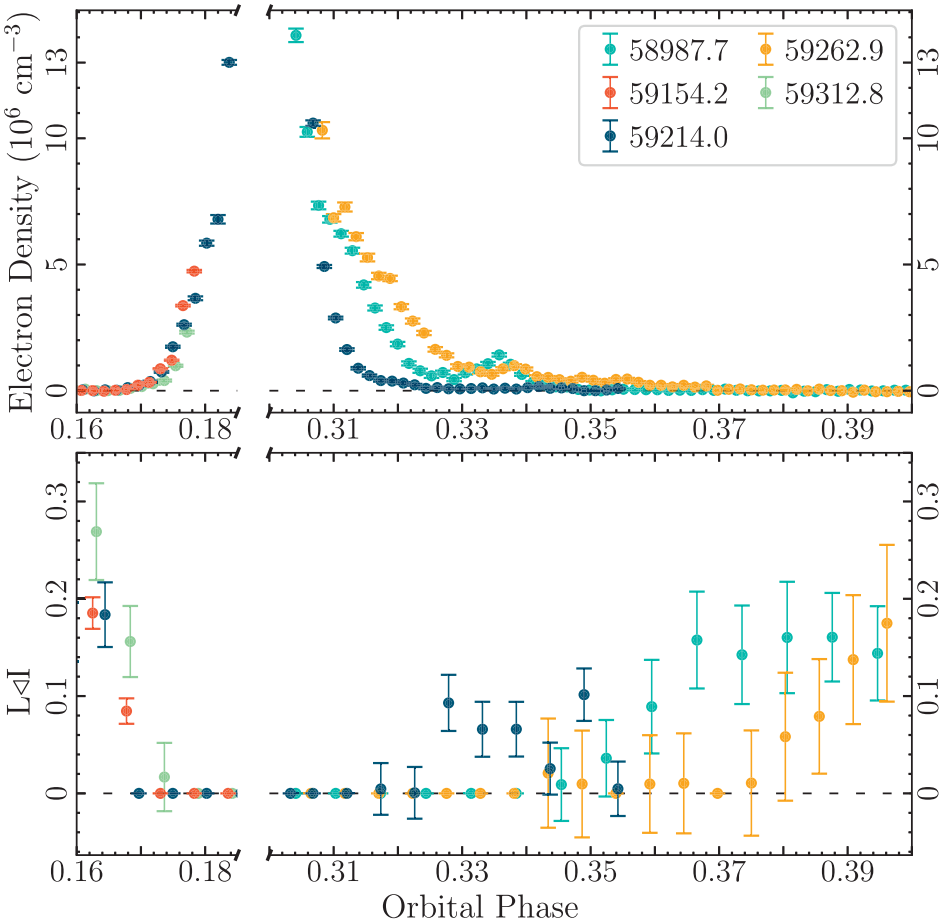

Figure 8. Upper panel: electron volume density at ingresses and egresses as a function of eclipse phase ϕ_b: $n_e(\phi_b) = 0.5 n_H R_E^{-1} \sin\phi_b^{-1} \left(\sin(\pi/2 - \phi_b) - \frac{1}{3}\sin(\pi/2 - \phi_b)^3\right)^{-1}$ assuming a wind density profile of $n_e \propto 1/r$, where r is the distance from the companion center, R_E is the eclipsing radius and n_H is the column density derived from the excess DM (Figure 6). Lower panel: A close-up of the liner polarization fraction at the eclipse ingresses and egresses.

The majority of energy in the pulsar wind is carried by relativistic particles. The magnetic fields in the pulsar wind could be much smaller than the magnetic field of the companion at the orbital distance. After all, the pulsar's magnetic field is only 1.6×10^8 G at its 10 km radius surface (Table 1). The pulsar wind is almost transparent to the pulsar emission. This is because of the low density and the high Lorenz factor of the wind particles. The wind particles have motion masses far exceeding their rest masses, causing their Faraday rotation effect to be negligible (Quataert & Gruzinov 2000; Wang et al. 2011). When a moderate amount of slow-moving ionized materials from the companion's magnetosphere flow out of the boundary and come to the pulsar wind side, the combination of the extra slow electrons and a reasonably low magnetic field (10 mG) environment leads to the incomplete depolarization and the Faraday rotation. As we mentioned in the previous section, such a condition is rarely met (only be observed in MJD 59 214). In most of the ingresses and egresses of this pulsar, the out-flowing electrons are either too dense or too variable and often completely depolarize the pulsar signal.

Thompson et al. (1994) predicted that the pulsar wind could contain an oscillating part around the eclipsing edge with an oscillation length of $cP/2 \simeq 500$ km, where c is the speed of light and P is the spin period of the pulsar. It should be noted that such reciprocating magnetic fields in the pulsar wind was already illustrated in the model of Phinney et al. (1988). But such field was never observed until now. We observed an oscillation length of 5×10^3 km, different from the prediction, possibly due to our viewing angle or the reconnection loop expanding due to pressure changes.

The pulsar wind is expected to contain an alternating magnetic field in both the radial and transverse directions. This means that the eclipse was due to plasma occupying a relatively

small volume of space in which the field is relatively uniform in the radial direction. It is possible that in the particular egress of MJD 59214, the eclipsing plasma was a small stream of matter escaping the magnetosphere. This might not be the case for the other egresses, through which significantly higher electron densities were observed and pulsar signals are completely depolarized.

The asymmetry between the depolarizing ingress and egress phase could be caused by an asymmetrical boundary shock layer deformed by orbit motion as illustrated in Figure 7(c). In our picture, the shock between the magnetized plasma is collisionless and could have boundaries with varying thickness depending on the conditions at the eclipse egresses.

We conclude that the companion magnetosphere plus pulsar wind picture could explain most of the observations. It also predicts that a shock boundary exists between the pulsar and the companion. Inside the shock boundary, the magnetic field could reach the $\gtrsim$10 G level required for pressure balance and intensity eclipse, outside the boundary both the electron density is $\sim 10^6$ cm^{-3} and the magnetic field is only $\sim$10 mG. As suggested by Wadiasingh et al. (2018), if sufficient dissipation and heating exist in this boundary, one may be able to observe double-peaked X-ray modulation like those observed in some low-mass millisecond pulsar binaries.

Acknowledgments

We would like to express our appreciation to the anonymous reviewer. This work has used the data from the Five-hundred-meter Aperture Spherical radio Telescope (FAST), Parkes 64 m "Murriyang" radio-telescope, and Green Bank Telescope (GBT). FAST is a Chinese national mega-science facility, operated by the National Astronomical Observatories of Chinese Academy of Sciences (NAOC). The Parkes Radio Telescope (Murriyang) is part of the Australia Telescope National Facility, which is funded by the Australian Government for operation as a National Facility managed by CSIRO. The Green Bank Observatory is a facility of the National Science Foundation (NSF) operated under cooperative agreement by Associated Universities, Inc. The National Radio Astronomy Observatory is a facility of the NSF operated under cooperative agreement by Associated Universities, Inc. This work is supported by the National Natural Science Foundation of China (NSFC) grant Nos. 12041303, 12041304, 11873067, 12133004, 12203045, 12203070, 12203072, 12103013, U2031117 and T2241020, the CAS-MPG LEGACY project and the National SKA Program of China No. 2020SKA0120200, the Foundation of Science and Technology of Guizhou Province No. ((2021)023), the Foundation of Guizhou Provincial Education Department (No.KY(2021)303), the National Key Research and Development Program of China Nos. 2022YFC2205202 and 2022YFC2205203, the Major Science and Technology Program of Xinjiang Uygur Autonomous Region Nos. 2022A03013-1, 2022A03013-3 and 2022A03013-4, the National Key Research and Development Program of China No. 2022YFC2205203 and the 2021 project Xinjiang Uygur autonomous region of China for Tianshan elites and the Youth Innovation Promotion Association of CAS under No. 2023069. P. Wang acknowledges support from the Youth Innovation Promotion Association CAS (id. 2021055), CAS Project for Young Scientists in Basic Research (grant YSBR-006) and the Cultivation Project for FAST Scientific Payoff and Research Achievement of CAMS-CAS. J.-b. Wang acknowledges support from Zhejiang Provincial Natural Science Foundation of China under grant No. LY23A030001. M. McLaughlin and V. Blackmon are supported by the NSF Physics Frontiers Center award number 2020265.

Appendix
Observation Parameters and Eclipsing Events

A table (Table A1) with the timing parameters of the observations and the eclipsing events. The "Observation MJD" column indicates the start time of the observation (to the minute), and the "Eclipsing" column indicates whether the eclipse was captured in this observation.

Table A1
Timing Observations of J1720−0534 and Eclipsing Events

Telescope	f_{center} (MHz)	Bandwidth (MHz)	n_{chan}	T_{samp} (μs)	Observation MJD	Observation Length (minutes)	Eclipsing Y/N
FAST	1250	500	1024	49.152	58987.7177	50	Y
FAST	1250	500	1024	49.152	58990.6943	200	Y
FAST	1250	500	1024	49.152	58993.6922	105	Y
FAST	1250	500	1024	49.152	58998.6783	105	N
FAST	1250	500	1024	49.152	59001.6781	5	N
FAST	1250	500	1024	49.152	59061.5563	5	N
FAST	1250	500	1024	49.152	59081.4489	10	N
FAST	1250	500	1024	49.152	59094.4285	10	N
FAST	1250	500	1024	49.152	59109.3841	10	N
FAST	1250	500	1024	49.152	59121.3556	10	N
FAST	1250	500	1024	49.152	59129.3276	10	N
FAST	1250	500	1024	49.152	59140.2981	10	N
FAST	1250	500	1024	49.152	59164.2306	10	N
FAST	1250	500	1024	49.152	59186.2083	15	N
FAST	1250	500	1024	49.152	59192.1847	15	N
FAST	1250	500	1024	49.152	59205.1752	5	N
FAST	1250	500	1024	49.152	59218.1414	15	N
FAST	1250	500	1024	49.152	59231.0423	15	N
FAST	1250	500	1024	49.152	59255.9701	10	N
FAST	1250	500	1024	49.152	59267.9802	10	Y
FAST	1250	500	1024	49.152	59304.8621	10	N
FAST	1250	500	1024	49.152	59335.7548	15	N
FAST	1250	500	1024	49.152	59427.5515	5	N
FAST	1250	500	1024	49.152	59439.5063	5	N
FAST	1250	500	1024	49.152	59443.4924	5	N
FAST	1250	500	1024	49.152	59456.4333	5	N
FAST	1250	500	1024	49.152	59466.3917	5	N
FAST	1250	500	1024	49.152	59469.3994	5	N
FAST	1250	500	1024	49.152	59476.4153	5	N
FAST	1250	500	1024	49.152	59494.3424	5	N
FAST	1250	500	1024	49.152	59509.3376	5	N
FAST	1250	500	8192	98.304	59139.3354	15	N
FAST	1250	500	8192	98.304	59154.2994	20	Y
FAST	1250	500	8192	98.304	59158.2786	20	Y
FAST	1250	500	8192	98.304	59212.1536	60	N
FAST	1250	500	8192	98.304	59214.0841	60	Y
FAST	1250	500	8192	98.304	59258.9811	15	N
FAST	1250	500	8192	98.304	59262.9751	40	Y
FAST	1250	500	8192	98.304	59297.8722	120	N
FAST	1250	500	8192	98.304	59312.8341	60	Y
FAST	1250	500	8192	98.304	59356.7170	60	Y
FAST	1250	500	8192	98.304	59583.0829	60	N
GBT	350	105	128	20.48	59626.6761	46	N
GBT	820	240	128	10.24	59309.3510	5	N
GBT	820	240	128	10.24	59312.4686	5	N
GBT	820	240	128	10.24	59316.4761	4	N
GBT	820	240	128	10.24	59607.5164	35	N
Parkes	2368	3328	3328	128	59588.0406	160	N

ORCID iDs

Chen-Chen Miao https://orcid.org/0000-0002-9441-2190
Jia-Rui Niu https://orcid.org/0000-0001-8065-4191
Zhi-Gang Wen https://orcid.org/0000-0003-2991-7421
Meng-Yao Xue https://orcid.org/0000-0001-8018-1830
Wen-Ming Yan https://orcid.org/0000-0002-7662-3875

References

Altamirano, D., Cavecchi, Y., Patruno, A., et al. 2011, ApJL, 727, L18
Cameron, A. D., Li, D., Hobbs, G., et al. 2020, MNRAS, 495, 3515
Crowter, K., Stairs, I. H., McPhee, C. A., et al. 2020, MNRAS, 495, 3052
Cruces, M., Champion, D. J., Li, D., et al. 2021, MNRAS, 508, 300
Eggleton, P. P. 1983, ApJ, 268, 368
Everett, J. E., & Weisberg, J. M. 2001, ApJ, 553, 341

Freire, P. C. C., & Ridolfi, A. 2018, MNRAS, 476, 4794
Fruchter, A. S., Stinebring, D. R., & Taylor, J. H. 1988, Natur, 333, 237
Gaia Collaboration, Brown, A. G. A., Vallenari, A., et al. 2021, A&A, 649, A1
Hobbs, G., Manchester, R. N., Dunning, A., et al. 2020, PASA, 37, e012
Hobbs, G. B., Edwards, R. T., & Manchester, R. N. 2006, MNRAS, 369, 655
Hotan, A. W., van Straten, W., & Manchester, R. N. 2004, PASA, 21, 302
Jiang, P., Tang, N.-Y., Hou, L.-G., et al. 2020, RAA, 20, 064
Kansabanik, D., Bhattacharyya, B., Roy, J., & Stappers, B. 2021, ApJ, 920, 58
Li, D., Bilous, A., Ransom, S., Main, R., & Yang, Y.-P. 2023, Natur, 618, 484
Li, D., Lin, F. X., Main, R., et al. 2019, MNRAS, 484, 5723
Li, D., Wang, P., Qian, L., et al. 2018, IEEE Microwave Mag., 19, 112
Miao, C. C., Zhu, W. W., Li, D., et al. 2023, MNRAS, 518, 1672
Nan, R., Li, D., Jin, C., et al. 2011, IJMPD, 20, 989
Nice, D., Demorest, P., Stairs, I., et al. 2015, Tempo: Pulsar timing data analysis, Astrophysics Source Code Library, ascl:1509.002
Phinney, E. S., Evans, C. R., Blandford, R. D., & Kulkarni, S. R. 1988, Natur, 333, 832
Polzin, E. J., Breton, R. P., Clarke, A. O., et al. 2018, MNRAS, 476, 1968
Polzin, E. J., Breton, R. P., Stappers, B. W., et al. 2019, MNRAS, 490, 889
Purcell, C. R., Van Eck, C. L., West, J., Sun, X. H., & Gaensler, B. M. 2020, RM-Tools: Rotation measure (RM) synthesis and Stokes QU-fitting, Astrophysics Source Code Library, ascl:2005.003
Quataert, E., & Gruzinov, A. 2000, ApJ, 545, 842
Radhakrishnan, V., & Cooke, D. J. 1969, ApL, 3, 225
Ransom, S. 2011, PRESTO: PulsaR Exploration and Search TOolkit, Astrophysics Source Code Library, ascl:1107.017
Reiners, A., & Christensen, U. R. 2010, A&A, 522, A13
Roberts, M. S. E. 2011, Radio Pulsars: An Astrophysical Key to Unlock the Secrets of the Universe in AIP Conf. Proc. 1357, ed. M. Burgay et al. (Melville, NY: AIP), 127
Roberts, M. S. E. 2013, in Neutron Stars and Pulsars: Challenges and Opportunities after 80 years, Vol. 291, ed. J. van Leeuwen (Cambridge: Cambridge Univ. Press), 127
Sckopke, N., Paschmann, G., Bame, S. J., Gosling, J. T., & Russell, C. T. 1983, JGR, 88, 6121
Thompson, C., Blandford, R. D., Evans, C. R., & Phinney, E. S. 1994, ApJ, 422, 304
van Straten, W., & Bailes, M. 2011, PASA, 28, 1
Wadiasingh, Z., Venter, C., Harding, A. K., Böttcher, M., & Kilian, P. 2018, ApJ, 869, 120
Wang, C., Han, J. L., & Lai, D. 2011, MNRAS, 417, 1183
Wang, S. Q., Wang, J. B., Wang, N., et al. 2021, ApJL, 922, L13
You, X. P., Manchester, R. N., Coles, W. A., Hobbs, G. B., & Shannon, R. 2018, ApJ, 867, 22